Biological imaging with 4D ultrafast electron microscopy

David J. Flannigan, Brett Barwick, and Ahmed H. Zewail[1]

Physical Biology Center for Ultrafast Science and Technology, Arthur Amos Noyes Laboratory of Chemical Physics, California Institute of Technology, Pasadena, CA 91125

Contributed by Ahmed H. Zewail, April 26, 2010 (sent for review April 17, 2010)

Advances in the imaging of biological structures with transmission electron microscopy continue to reveal information at the nanometer length scale and below. The images obtained are static, i.e., time-averaged over seconds, and the weak contrast is usually enhanced through sophisticated specimen preparation techniques and/or improvements in electron optics and methodologies. Here we report the application of the technique of photon-induced near-field electron microscopy (PINEM) to imaging of biological specimens with femtosecond (fs) temporal resolution. In PINEM, the biological structure is exposed to single-electron packets and simultaneously irradiated with fs laser pulses that are coincident with the electron pulses in space and time. By electron energy-filtering those electrons that gained photon energies, the contrast is enhanced only at the surface of the structures involved. This method is demonstrated here in imaging of protein vesicles and whole cells of *Escherichia coli*, both are not absorbing the photon energy, and both are of low-*Z* contrast. It is also shown that the spatial location of contrast enhancement can be controlled via laser polarization, time resolution, and tomographic tilting. The high-magnification PINEM imaging provides the nanometer scale and the fs temporal resolution. The potential of applications is discussed and includes the study of antibodies and immunolabeling within the cell.

evanescent | nanoscale | biostructure

The development and application of imaging techniques for the visualization of biological structures continues to advance our understanding of such systems. Various optical techniques have been developed to improve the spatial resolution beyond the diffraction limit (1–3) and to study, e.g., protein folding and adhesion complexes in living cells (4, 5). Though powerful, most optical methods rely on molecular components that emit light (fluoresce) and the spatial resolution cannot yet rival that of electron-based techniques that allow focusing down to the atomic scale (6). Force probe microscopies have been used to image surfaces of cells and porosomes with high enough spatial resolution (7), and pulsed X-ray sources, such as synchrotrons and free-electron lasers, hold promise for femtosecond (fs) diffraction studies of individual biological macromolecules (8). Biological imaging with electron microscopy goes back to the 1960s and has since then been advanced to enable structural mapping (9) of biological macromolecules and cells (10–12), including viruses and molecular machines such as the ribosome (6, 13).

The visualization of biological structures with an electron microscope presents unique challenges, especially when considering the inherent weak contrast associated with such structures. This weak contrast, which is primarily because of the low-*Z* (atomic number) elemental composition of biological specimens and the need for thin samples, is often addressed by employing sophisticated specimen preparation techniques (e.g., ultrathin sectioning and staining) and by increasing the coherence of the electron beam and manipulation of the contrast transfer function. In modern electron microscopes, highly coherent beams are used in conjunction with energy filtering to enhance contrast and produce element-specific spatial maps of, e.g., cell nuclei (12). In combination with tomography, the energy-filtering method can now be used to image the elemental composition of whole unstained cells in the three spatial dimensions (11). For such static images, direct access to the fourth dimension—time—is not possible, and the contrast is determined by the degree of interaction between the electrons and the specimen.

The development of ultrafast electron microscopy (UEM) at Caltech provides a means to access the four dimensions with high spatial and temporal resolutions (6, 14). Prior applications of UEM have been concerned with the visualization of structural and morphological dynamics, including studies of atomic motions and phase transitions, chemical binding, and nanomechanical motions (15–17). Biological imaging with UEM has thus far included investigations of stained epithelial cells (18), cryoprepared bacterial cells (*Caulobacter crescentus*), and cryocatalase protein crystals at high resolution (14), all taken as snapshots with fs electron pulses and by using either amplitude or phase contrast methods. Thus, for these examples of biological UEM imaging photons were involved neither in clocking the change nor for the enhancement of the contrast.

Recently, we reported a variant of UEM imaging, dubbed photon-induced near-field electron microscopy (PINEM) (19), and demonstrated that the teaming of photons and electrons in the microscope provides nanometer spatial and fs temporal resolutions with enhanced contrast. This near-field method is selective to fields of structures whose dimensions are orders of magnitude smaller than the diffraction limit and provides unique polarization and temporal features. Earlier (19), PINEM was applied to carbon nanotubes and silver nanowires. Here we report the PINEM imaging of two biological structures: the outer shell of liquid-filled protein vesicles and cell structure of whole *Escherichia coli*. The key concept here involves the filtering of electron energy only in the gain region—i.e., when the electron acquires photon energy—not, as conventionally done, by using the loss region when the electron gives up its energy to the specimen. This way the contrast "lights up" and the fs temporal response is resolved. Because imaging of evanescent fields enhances the contrast, the spatial location of the enhancement can be controlled via laser polarization, time scale, and tomographic tilting. Finally, we note that the intrinsic properties of biological systems differ greatly from the inorganic ones previously studied, yet PINEM is still possible, thus suggesting the applicability of the technique to a wide range of structures.

Results and Discussion

Concept of PINEM. Before the imaging results are discussed, we provide here a brief description of the discrete electron energy gain and loss in UEM and the concept of PINEM. Typically, the passage of an electron through a thin specimen results in the kinetic energy being either conserved (elastic) with only momentum change or reduced (inelastic) through the excitation of the specimen. In electron microscopy, both types of scattered

Author contributions: D.J.F., B.B., and A.H.Z. designed research, performed research, contributed new reagents/analytic tools, analyzed data, and wrote the paper.

The authors declare no conflict of interest.

[1]To whom correspondence should be addressed. E-mail: zewail@caltech.edu.

electrons can be used to form an image, the appearance of which depends upon the specific atomic structure and composition of the specimen. In addition, the element-specific electron scattering provides a means to generate a chemical map of the sample region of interest with high resolution (20). These types of scattering events produce losses of probing electron energies, corresponding to the energies of the atomic core electrons. The so-called "low-loss region" near the (elastic) zero-loss energy pertains to those electrons that have lost only a small amount of kinetic energy, typically because of interactions with valence electrons and bulk and surface plasmons.

The above description involving the energy loss (or no loss) forms the basis for electron microscopy imaging in various domains. What was not expected was the gain of energy by the electron; when a fs laser pulse and an ultrashort electron packet are overlapped in space and time at a nanostructure in situ, a unique region of energy gain is observed (19). The interaction between the photon and electron at the nanostructure results in the 200-keV electrons gaining n quanta of photon energy; in other words, the electron absorbs, instead of emitting, the photon energy. Both the absorption and emission of light by the electrons produce peaks in the energy spectrum, and these peaks are located in the gain and loss regions at integer multiples of the photon energy. For PINEM, the electrons that have absorbed photons are selected by energy filtering, and an image that shows precisely where the gain events have occurred can be formed. Only electrons that travel near the structure absorb photons, and thus with this filtering in the gain region we can reach high resolution in contrast and without interference from background because of contrast of the elastic and loss regions—i.e., an enhancement of the nanoscale contrast.

Fig. 1 displays the region of the electron energy spectrum taken when the spatiotemporal overlap of the fs laser pulse and electron packet is optimum at a single protein vesicle and when they separate temporally by +1 ps. As can be seen, the $t = 0$ spectrum shows loss and gain peaks occurring at integer multiples of the photon energy, whereas the $t = +1$ ps spectrum does not, similar to what was observed for nonbiological materials (19). Whereas

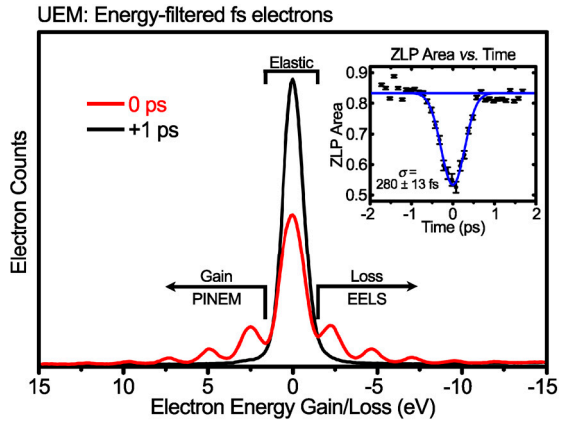

Fig. 1. Femtosecond time dependence of electron energy spectra of a protein vesicle. A spectrum obtained at 0 ps (i.e., when the spatiotemporal overlap of the laser pulse and electron packet at the vesicle is at a maximum, shown in red) is compared to a spectrum obtained at +1 ps (i.e., when the electron packet arrives at the vesicle 1 ps after the fs laser pulse, shown in black). The electron energy gain (PINEM) and loss (electron energy loss spectrometry, EELS) regions, which are comprised of sidebands occurring at integer multiples of the fs laser photon energy, are labeled, as is the elastic scattering region (i.e., the ZLP). The inset displays the temporal response of the ZLP area (normalized to the integrated area of the entire spectrum, black data points) and a least-squares Gaussian fit (solid blue). The error bars represent two standard errors of the mean. Here, the FWHM of the Gaussian fit is 670 ± 30 fs, which gives a standard deviation (σ) of 280 ± 13 fs, with the errors representing one standard error of the mean. The photon pulses are ~250 fs.

all regions of the spectrum can be selected and used to generate images, only those electrons that have gained energy—the gain region—are used in PINEM; the elastic and loss regions are used for conventional imaging of the same specimen, e.g., in the bright-field mode. Thus, the spatial characteristics of the gain process can be directly visualized, as discussed below. In Fig. 1 (*Inset*) the fs temporal response of both the electron and photon pulses is shown as the change in the area of the zero-loss peak (ZLP) as a function of time, illustrating the feasibility of visualizing ultrafast dynamics with this technique; the fitted response gives $\sigma = 280 \pm 13$ fs (see Fig. 1 and *Materials and Methods*).

Imaging of Protein Vesicles. We now present the results of PINEM imaging of individual biological structures, biomimetic protein vesicles; the results from whole unstained *E. coli* cells are discussed below. Fig. 2 displays a bright-field transmission electron microscopy (TEM) and a PINEM image of a typical specimen of protein vesicles. The vesicles are composed of a shell of covalently cross-linked BSA protein molecules encapsulating a liquid core (21) and are useful as biomimetic cellular structures (22) as well as for a wide range of practical purposes (e.g., drug delivery and contrast agents) (23–25). The cross-linking is achieved through the formation of interprotein sulfur-sulfur bonds via oxidation of cysteine residues in the BSA molecules, and the structure of the individual particles is not highly denatured during vesicle formation (23). Therefore, a 500-nm vesicle with a 50-nm-thick shell will be comprised of ~500,000 individual BSA protein molecules, each of which occupies ~60 nm^3 (26).

As discussed above, a PINEM image of a vesicle is formed by filtering the electrons such that only those that have gained energy because of the PIN effect are used; the image is generated at the maximum spatiotemporal overlap of the laser pulse and electron packet (i.e., $t = 0$). Shown in Fig. 2 is the PINEM imaging of the vesicle that produces enhanced contrast at the edge, where the protein shell resides, relative to the remainder of the field of view. That is, the intensity far from the structure being visualized in a typical bright-field image, which is responsible for the weakened contrast, is not present in PINEM. Here the effect shown in the images is the result of fields created by the dielectric (protein) shell, relative to vacuum, by the fs laser pulse. This evanescent electric field at the surface of the vesicle is unique to nanostructures, and its strength decays exponentially with distance (19).

Beyond the enhanced contrast provided by PINEM, and perhaps most importantly, the UEM methodology allows for the fs temporal response of the PIN effect to be directly visualized and controlled. By changing the delay between the excitation

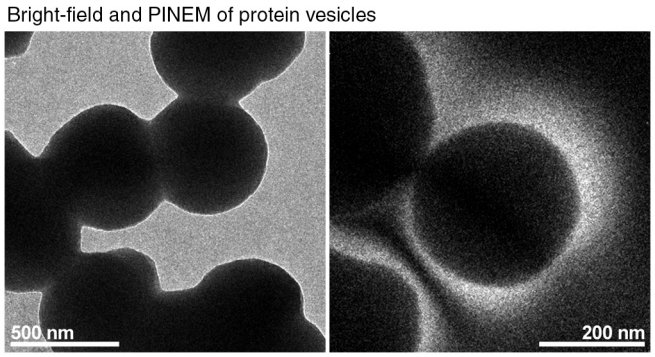

Fig. 2. Bright-field TEM image (*Left*) and PINEM image (*Right*) of protein vesicles. The bright-field (BF) image was obtained at a magnification of 27,500×, whereas the PINEM image was obtained at a magnification of 67,000×. The PINEM image was recorded at the maximum spatiotemporal overlap of the fs laser pulse and electron packet. The raw PINEM image was filtered for noise removal, and the border around the vesicles in the BF image is because of the slight defocus of the lens.

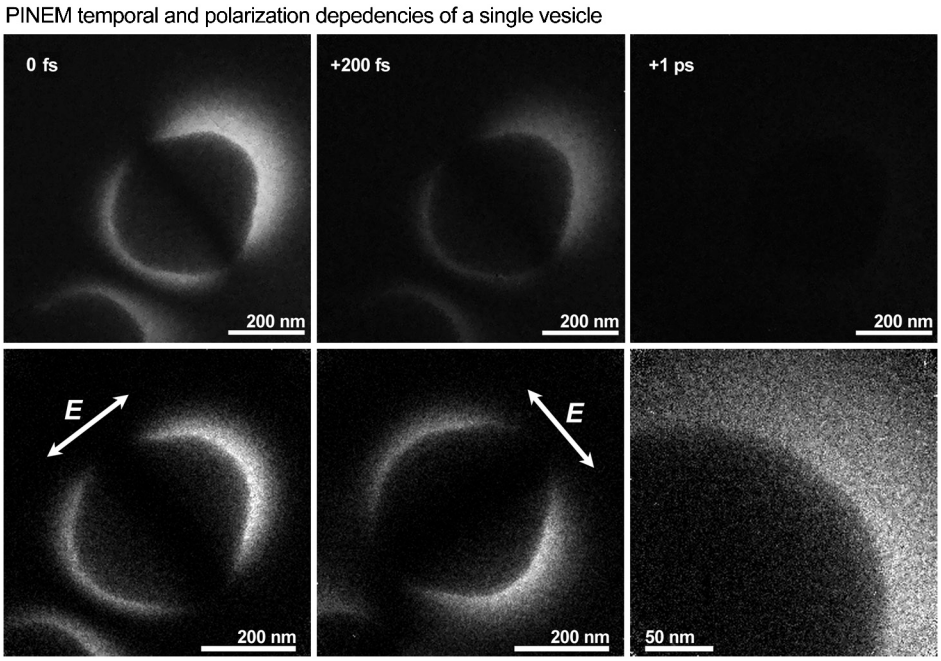

Fig. 3. Ultrafast, polarization, and high-magnification PINEM imaging of a single protein vesicle. Shown in the top row are three PINEM images of the same protein vesicle, but obtained at different points in time (0 fs, +200 fs, and +1 ps). Each image was acquired at a magnification of 53,000×. Each image was filtered for noise removal, and the contrast limits are all set to the same range. The bottom row displays PINEM images of a protein vesicle generated with the fs laser light linearly polarized in a plane indicated by the double-headed arrows (left and center), as well as a PINEM image of a portion of a protein vesicle obtained at high magnification (right). The polarization images were obtained at a magnification of 67,000×, whereas the high-magnification image was obtained at 200,000×. Each pixel in the high-magnification image corresponds to 8.8 Å. The raw images were filtered for noise removal.

laser pulse and the ultrashort electron packet impinging on the protein vesicle, the time dependence of the interaction can be followed, as shown in Fig. 3. The response is remarkably ultrafast, with the PINEM contrast being significantly weaker after only 200 fs and essentially being zero at ±1 ps. The timing of the response in the PINEM images is consistent with that quantified from the ZLP of a single protein vesicle (Fig. 1, *Inset*). Clearly, imaging the fields of concern here requires ultrashort time scales.

The controllability and high-spatial resolution capabilities of the PINEM technique for biological imaging are displayed in Fig. 3. As can be seen, the spatial location of the PIN effect around the structure is accomplished by changing the orientation of the plane of polarization of the fs laser pulse with respect to the vesicle orientation. The location of the gain regions appears as diametrically opposed contrast enhancements, the specific locations of which precisely follow the laser polarization. A high-magnification PINEM image (pixel size = 8.8 Å) of one side of a protein vesicle demonstrates the potential to visualize single cellular particles being tens of nanometers in diameter (e.g., ribosomes), but with the accompanying fs temporal resolution and enhanced contrast capabilities afforded by the technique. It is important to note here that the PINEM signal scales with the number of laser photons impinging upon the specimen. Because the vesicles do not absorb the 532-nm laser light, substantial fluences can be used to form images without causing photothermal damage.

Imaging of Whole Unstained *E. coli* Cells. To determine the feasibility of using PINEM to image biological structures with increased complexity relative to simple protein vesicles, we chose to study whole unstained and unfixed cells of the common bacteria *E. coli*. Whereas the *E. coli* cells are much more complex than a simple vesicle, they are ideal model systems for demonstrating biological imaging with PINEM. One reason for this is that they are prokaryotes and thus lack the intracellular complexity of eukaryotic cells (e.g., a membrane-bound nucleus, mitochondria, Golgi bodies, etc.). Another reason is that the *E. coli* cell has been extensively imaged with electron microscopy, and several high-resolution studies of the ultrastructure have been published (27, 28).

In the bright-field (Fig. 4), typical images display the mass-thickness contrast of the cell and with some variations within the cell. The nucleoid (i.e., DNA material) is visible in the upper portion of the cell as a dark (thick) region, as are many small particles of ~20 nm diameter, presumably ribosomes, dispersed throughout the cytoplasm. We also observe the cellular envelope—i.e., the material comprising the outer and cytoplasmic membranes. Indeed, the ~50 nm gap between the outer and cytoplasmic membranes, which contained the peptidoglycan layer, is visible. As can be seen in Fig. 4, PINEM imaging of whole unstained and unfixed cells is demonstrated; the images were generated by maximizing the spatiotemporal overlap of the fs laser pulse and electron packet at the specimen.

It is worth pointing out several interesting features of the PINEM images. Unlike the protein vesicles discussed above, enhanced contrast is observed at both the outer and inner regions of the cell, which is because portions of the cell are thin relative to the thick liquid-filled vesicles, the result of which is similar to thickness contrast in bright-field TEM and UEM images. The PINEM images illustrate that electrons passing through the thinner regions of the cell experience gains and losses near intracellular topological features, a result that bodes well for imaging ultrastructure with this technique.

Next we examined the time scale of the PINEM of the cells. By changing the delay time between the fs laser pulse and electron packet incident at the cell, the time dependence of the image was

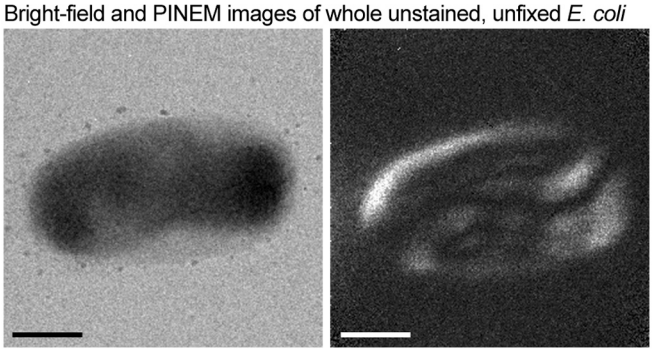

Fig. 4. Bright-field TEM and PINEM images of a whole unstained and unfixed *E. coli* cell. Both images were obtained at a magnification of 19,000×. The PINEM image was filtered for noise removal. (Scale bars, 500 nm.)

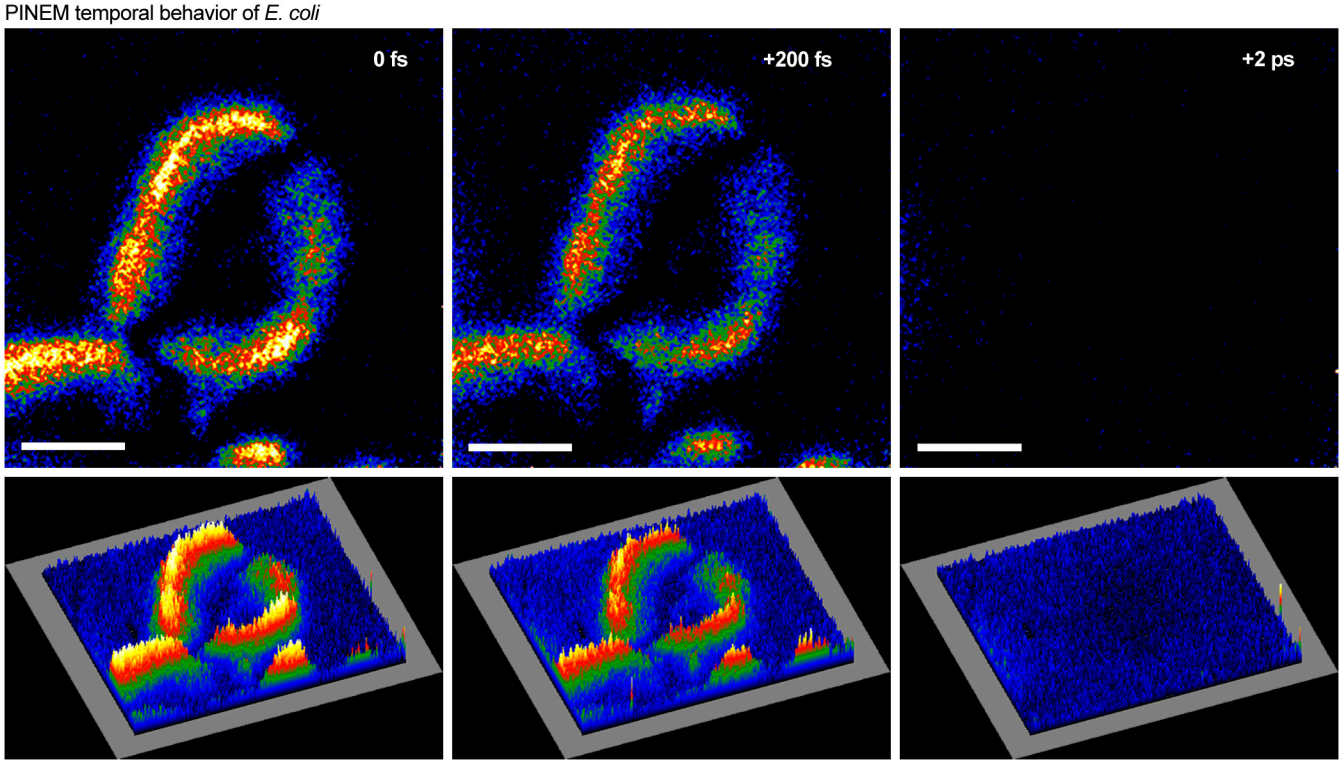

Fig. 5. Ultrafast PINEM imaging of a whole unstained and unfixed *E. coli* cell. Shown are three pseudocolor PINEM images (top row) and the corresponding three-dimensional surface plots (bottom row) of the same cell, but obtained at different points in time (0 fs, +200 fs, and +2 ps). Each image was acquired at a magnification of 53,000×, and all were filtered for noise removal. The contrast limits are set to the same range for each row of images. (Scale bars, 500 nm.)

followed (Fig. 5), just as was the case with the (dielectric) protein vesicles (Fig. 3) and inorganic conducting materials (19). Again, the response is ultrafast, with the contrast weakening within 200 fs of maximum laser pulse and electron packet overlap. Thus, the observed enhancement is optimum in UEM.

Finally, we studied tomographic-type images and the effect of photon polarization. Shown in Fig. 6 are PINEM images taken at different specimen tilt angles, which here were 0 and ±30°. One can see that as the tilt angle of the specimen is changed, the spatial distribution and strength of contrast varies. In conventional electron tomography, images obtained at different specimen tilt angles can be combined to construct 3D images of biological macromolecules (29), with the added capability of energy filtering for generating element-specific 3D maps (11). The PINEM images obtained at different tilt angles demonstrate that the technique could be used to generate similar tomographic images, but with the added capabilities of enhanced contrast and ultrafast temporal resolution. The polarization effect is evident in the results of Fig. 6 and is consistent with the concept of nanoscale directional change of the field.

Conclusions and Outlook. In this contribution, contrast enhancement in imaging, achieved with PINEM, has been shown to be possible for both biomimetic protein vesicles and whole unstained, unsliced, and unfixed cells. This advance enables the visualization of single particles of nanometer-scale dimensions, but with the added capability of fs temporal resolution. The controllability of PINEM imaging of biological structures, through the laser pulse polarization and specimen tilting, adds two other dimensions for selectivity in imaging. Currently, we are exploring the use of PINEM to image targeted sites of antibodies with immunolabeling (30) and the possibility of now varying a second time delay to examine dynamics with various specimen preparations, including cryogenic and even possibly biostructures at near-ambient conditions (31). It is also possible to vary the photon wavelength to map different dimensions, to further improve the spatial resolution by near-resonance confinement of the particle field, which is currently of 1- to 2-nm length scale (32), and the energy resolution for mapping all structures at once (33, 34). The properties of the biological systems differ significantly from the inorganic materials previously studied (19), yet imaging with PINEM is still possible, suggesting possible extensions to a wide range of materials (ref. 35 and references therein).

Materials and Methods

UEM and PINEM Methodologies. All experiments were done by using the second generation ultrafast electron microscope (UEM-2) within the Physical Biology Center at Caltech (36). The UEM methodology can be adjusted to suit a wide range of experimental requirements, and the interested reader is referred to previous works for additional details (14, 37, 38). The specific configuration used for the work reported here is now described. The electron microscope of UEM-2 is operated at 200 kV and equipped with a Gatan Imaging Filter and a 4 megapixel Ultrascan 1000 CCD camera. The microscope is interfaced with a fiber oscillator/amplifier laser system. The laser is configured to output 1,040 nm light of fs pulses. The 1,040 nm fundamental is frequency doubled (520 nm) and quadrupled (260 nm) for in situ specimen excitation and single electron per pulse generation, respectively. Here the repetition rate of the laser was varied between 1.4 and 1.55 MHz. All PINEM cell images were acquired with a specimen excitation fluence of 1.3 mJ/cm^2 (50 μm FWHM), and electron energy gain/loss spectra and PINEM images of the protein vesicle were obtained with an excitation fluence of 5.4 mJ/cm^2. PINEM images are generated by energy filtering and using only the gain region of the spectrum (19). After locating the maximum spatiotemporal overlap of the fs laser pulse and electron packets at the specimen, PINEM is achieved by setting a slit width of 10 eV and sequentially stepping the spectrum offset by 1-eV increments until only the gain region is selected (i.e., no part of the ZLP or loss region contributes to the energy-filtered images). The ZLP intensity as a function of the delay time provides the temporal response; given the response time of the dielectric protein shell and the optical pulse width (~250 fs), the observed response with $\sigma = 280 \pm 13$ fs conclusively indicate the fs nature of the electron pulse and the

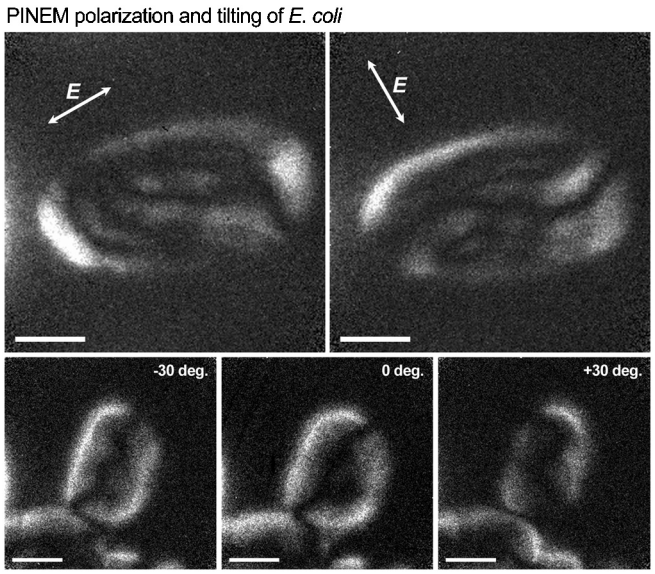

Fig. 6. Polarization and tomographic-type PINEM images of whole unstained and unfixed *E. coli* cells. The top row displays PINEM images of an *E. coli* cell generated with the fs laser light linearly polarized in a plane indicated by the double-headed arrows. The polarization images were obtained at a magnification of 19,000×. The raw images were filtered for noise removal. The bottom row displays a series of PINEM images obtained at different specimen tilt angles, which are shown in the upper right corner of each frame. The images were obtained at a magnification of 53,000× at the maximum spatiotemporal overlap of the fs laser pulse and electron packet. The raw PINEM images were filtered for noise removal, and the contrast limits are set to the same range. (Scale bar, 500 nm in all images shown.)

ultrashort response of PINEM. All experiments were performed in the single-electron regime; see ref. 14 for more details.

Synthesis of Protein Vesicles and Preparation of Specimens for UEM. Synthesis of the protein vesicles was done following the methodology developed by Suslick and co-workers (21, 39). Specifically here, BSA (Sigma-Aldrich, ≥98%) was dissolved in nanopure water (Barnstead, 18 MΩ · cm) at 5% wt/vol ratio. Toluene (EMD Chemicals, 99.99%) was layered on top of the aqueous protein solution at a 2:3 volume ratio such that the total liquid volume of the biphasic system was 30 mL. The reaction vessel was submerged in an ice water bath, and the tip of a Branson Sonifier 200 sonicator (20 kHz, 150 W, 1 cm tip diameter) was placed into the biphasic system at the interface between the organic and aqueous phases. The system was sonicated for 3 min at 33 W, which resulted in 24 W/cm^2 of acoustic power being transferred to the system, as determined with calorimetry and an initial temperature of 5.0 °C. After sonication, the product was washed with nanopure water and centrifuged at 6,000 rpm to separate the protein vesicles from the denser aqueous phase, which was removed and discarded. This washing and centrifuging step was repeated several times. The final purified vesicles were stored at 5 °C. A UEM specimen was prepared by placing a droplet (3 μL) of the purified vesicles suspended in nanopure water onto a 25-nm-thick silicon oxide TEM membrane grid (SiMPore, Inc.) and allowed to air dry.

The *E. coli* cell UEM specimen was prepared as follows. *E. coli* cells from acetone powder (Sigma, strain ATCC 12795) were dispersed in nanopure water (0.7 mg powder in 1 mL water). A droplet (3 μL) of the mixture was then placed onto a silicon oxide TEM membrane grid (SiMPore, Inc., 20 nm thick), which was cleaned before specimen preparation with an Ar plasma for 2 min. The specimen was allowed to air dry before analysis. Once dry, the specimen was immediately analyzed for cell coverage and structure.

ACKNOWLEDGMENTS. We thank Prof. M. R. Hoffmann for use of the sonicator. This work was supported by the National Science Foundation, the Air Force Office of Scientific Research, and the National Institutes of Health in the Center for Physical Biology supported by the Gordon and Betty Moore Foundation Caltech.

1. Hell SW (2007) Far-field optical nanoscopy. *Science* 316:1153–1158.
2. Huang B, Bates M, Zhuang XW (2009) Super-resolution fluorescence microscopy. *Annu Rev Biochem* 78:993–1016.
3. Min W, et al. (2009) Imaging chromophores with undetectable fluorescence by stimulated emission microscopy. *Nature* 461:1105–1109.
4. Ebbinghaus S, Dhar A, McDonald JD, Gruebele M (2010) Protein folding stability and dynamics imaged in a living cell. *Nat Methods* 7:319–323.
5. Shroff H, Galbraith CG, Galbraith JA, Betzig E (2008) Live-cell photoactivated localization microscopy of nanoscale adhesion dynamics. *Nat Methods* 5:417–423.
6. Zewail AH, Thomas JM (2010) *4D Electron Microscopy: Imaging in Space and Time* (Imperial College, London).
7. Jena BP, Hörber JKH, eds. (2002) *Atomic Force Microscopy in Cell Biology* (Academic, London).
8. Chapman HN (2009) X-ray imaging beyond the limits. *Nat Mater* 8:299–301.
9. Thomas JM (2008) *Physical Biology: From Atoms to Medicine*, ed AH Zewail (Imperial College, London), pp 51–114.
10. Leis A, Rockel B, Andrees L, Baumeister W (2009) Visualizing cells at the nanoscale. *Trends Biochem Sci* 34:60–70.
11. Leapman RD, Kocsis E, Zhang G, Talbot TL, Laquerriere P (2004) Three-dimensional distributions of elements in biological samples by energy-filtered electron tomography. *Ultramicroscopy* 100:115–125.
12. Bazett-Jones DP, Hendzel MJ, Kruhlak MJ (1999) Stoichiometric analysis of protein- and nucleic acid-based structures in the cell nucleus. *Micron* 30:151–157.
13. Glaeser RM, Downing K, DeRosier D, Chiu W, Frank J (2007) *Electron Crystallography of Biological Macromolecules* (Oxford Univ Press, New York).
14. Zewail AH (2010) Four-dimensional electron microscopy. *Science* 328:187–193.
15. Barwick B, Park HS, Kwon OH, Baskin JS, Zewail AH (2008) 4D imaging of transient structures and morphologies in ultrafast electron microscopy. *Science* 322:1227–1231.
16. Carbone F, Kwon OH, Zewail AH (2009) Dynamics of chemical bonding mapped by energy-resolved 4D electron microscopy. *Science* 325:181–184.
17. Flannigan DJ, Samartzis PC, Yurtsever A, Zewail AH (2009) Nanomechanical motions of cantilevers: Direct imaging in real space and time with 4D electron microscopy. *Nano Lett* 9:875–881.
18. Lobastov VA, Srinivasan R, Zewail AH (2005) Four-dimensional ultrafast electron microscopy. *Proc Natl Acad Sci USA* 102:7069–7073.
19. Barwick B, Flannigan DJ, Zewail AH (2009) Photon-induced near-field electron microscopy. *Nature* 462:902–906.
20. Egerton RF (1996) *Electron-Energy Loss Spectroscopy in the Electron Microscope* (Plenum, New York).
21. Suslick KS, Grinstaff MW (1990) Protein microencapsulation of nonaqueous liquids. *J Am Chem Soc* 112:7807–7809.
22. Fendler JH (1980) Surfactant vesicles as membrane mimetic agents: Characterization and utilization. *Acc Chem Res* 13:7–13.
23. Toublan FJ-J, Boppart S, Suslick KS (2006) Tumor targeting by surface-modified protein microspheres. *J Am Chem Soc* 128:3472–3473.
24. Lee TM, et al. (2003) Engineered microsphere contrast agents for optical coherence tomography. *Opt Lett* 28:1546–1548.
25. Keller MW, Feinstein SB, Briller RA, Powsner SM (1986) Automated production and analysis of echo contrast agents. *J Ultrasound Med* 5:493–498.
26. Huang BX, Kim HY, Dass C (2004) Probing three-dimensional structure of bovine serum albumin by chemical cross-linking and mass spectrometry. *J Am Soc Mass Spectrom* 15:1237–1247.
27. Zhang PJ, Khursigara CM, Hartnell LM, Subramaniam S (2007) Direct visualization of *Escherichia coli* chemotaxis receptor arrays using cryo-electron microscopy. *Proc Natl Acad Sci USA* 104:3777–3781.
28. Salje J, Zuber B, Löwe J (2009) Electron cryomicroscopy of *E coli* reveals filament bundles involved in plasmid DNA segregation. *Science* 323:509–512.
29. Briegel A, et al. (2009) Universal architecture of bacterial chemoreceptor arrays. *Proc Natl Acad Sci USA* 106:17181–17186.
30. Roth J, Bendayan M, Orci L (1978) Ultrastructural localization of intracellular antigens by the use of protein A-gold complex. *J Histochem Cytochem* 26:1074–1081.
31. de Jonge N, Peckys DB, Kremers GJ, Piston DW (2009) Electron microscopy of whole cells in liquid with nanometer resolution. *Proc Natl Acad Sci USA* 106:2159–2164.
32. Maier SA, Atwater HA (2005) Plasmonics: Localization and guiding of electromagnetic energy in metal/dielectric structures. *J Appl Phys* 98:011101.
33. Colliex C, et al. (2009) Multi-dimensional and multi-signal approaches in scanning transmission electron microscopes. *Philos Trans R Soc A* 367:3845–3858.
34. Yurtsever A, Weyland M, Muller DA (2006) Three-dimensional imaging of nonspherical silicon nanoparticles embedded in silicon oxide by plasmon tomography. *Appl Phys Lett* 89:151920.
35. García de Abajo FJ (2009) Photons and electrons team up. *Nature* 462:861–862.
36. Park HS, Baskin JS, Kwon OH, Zewail AH (2007) Atomic-scale imaging in real and energy space developed in ultrafast electron microscopy. *Nano Lett* 7:2545–2551.
37. Park HS, Baskin JS, Barwick B, Kwon OH, Zewail AH (2009) 4D ultrafast electron microscopy: Imaging of atomic motions, acoustic resonances, and moiré fringe dynamics. *Ultramicroscopy* 110:7–19.
38. Kwon OH, Barwick B, Park HS, Baskin JS, Zewail AH (2008) 4D visualization of embryonic, structural crystallization by single-pulse microscopy. *Proc Natl Acad Sci USA* 105:8519–8524.
39. Suslick KS, Grinstaff MW, Kolbeck KJ, Wong M (1994) Characterization of sonochemically prepared proteinaceous microspheres. *Ultrason Sonochem* 1:S65–S68.